

Linking Micellar Structures to Hydrogelation for Salt-triggered Dipeptide Gelators

Andre Zamith Cardoso,^a Laura L. E. Mears,^a Beatrice N. Cattoz,^b Peter C. Griffiths,^b Ralf Schweins^c and Dave J. Adams^{a,*}

^a Department of Chemistry, University of Liverpool, Crown Street, Liverpool, L69 7ZD, U.K.

^b Department of Pharmaceutical, Chemical and Environmental Science, University of Greenwich, Medway Campus, Central Avenue, Chatham Maritime, Kent ME4 4TB, U.K.

^c Institut Laue-Langevin, Large Scale Structures Group, 71 Avenue des Martyrs, CS 20156, F-38042 Grenoble CEDEX 9, France

Supplementary Information

Index

1. Properties of the 2NapFF Solutions

1.1 ¹H-NMR and UV-Vis Spectroscopy of the solution phase

1.2 Viscosity Measurements

1.3 Frequency Sweeps

1.3.1 Analysis of Solution Frequency Sweeps

1.4 Strain Sweeps

1.4.1 Analysis of Solution Strain Sweeps

2. Properties of the 2NapFF Ca-hydrogels

2.1 Frequency sweeps

2.1.1 Analysis of Hydrogel Frequency Sweeps

2.2 Strain sweeps

2.2.1 Analysis of Hydrogel Strain Sweeps

2.3 Recovery tests of the Ca-hydrogels

2.3.1 Analysis of Hydrogel Recovery tests

3. FTIR of 2NapFF Solutions and Ca-hydrogels

4. Confocal Microscopy of the Ca-hydrogels

5. SEM images of the Ca-hydrogels

6. Small angle neutron scattering (SANS) of 2NapFF Solutions and Ca-hydrogels

1. Properties of the 2NapFF Solutions

1.1 ^1H -NMR and UV-Vis Spectroscopy of the solution phase

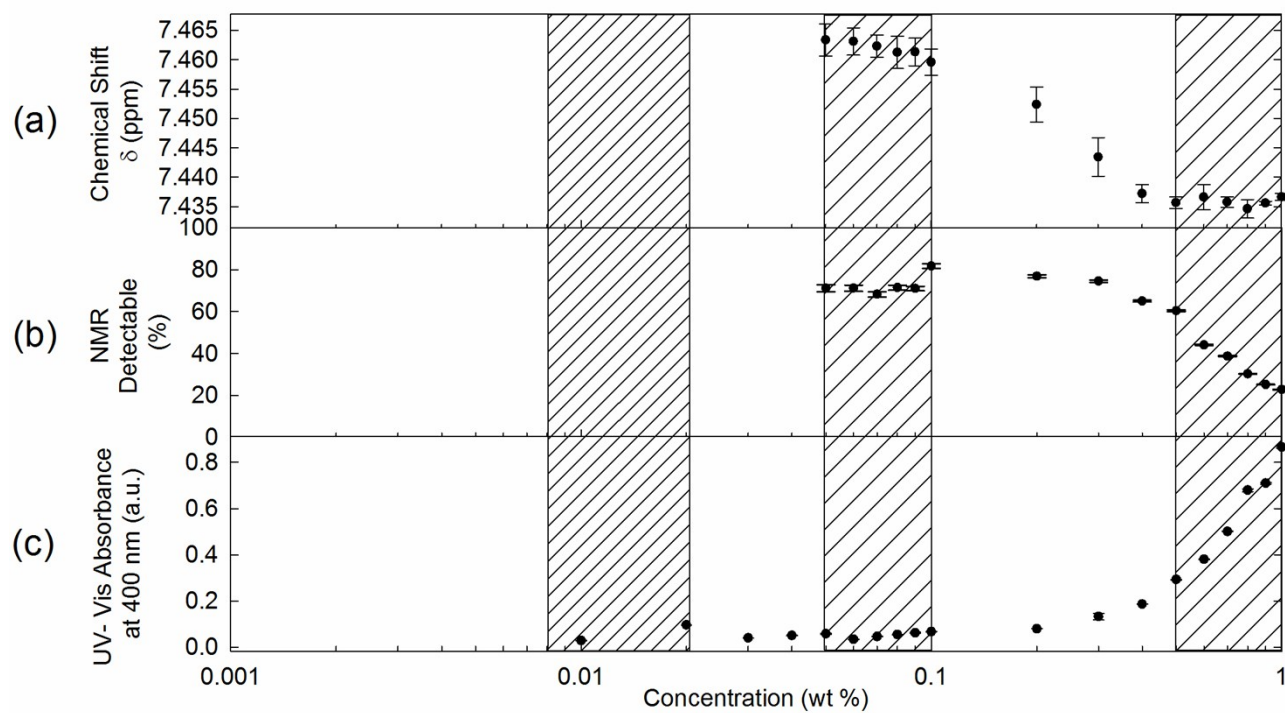


Figure S1. ^1H -NMR and UV-Vis spectroscopy analysis of the micellar solutions of 2NapFF at pH 10.5 ± 0.5 .

1.2 Viscosity Measurements

The viscosity data are separated for lower (a) and higher concentration (b) in Fig. S2.

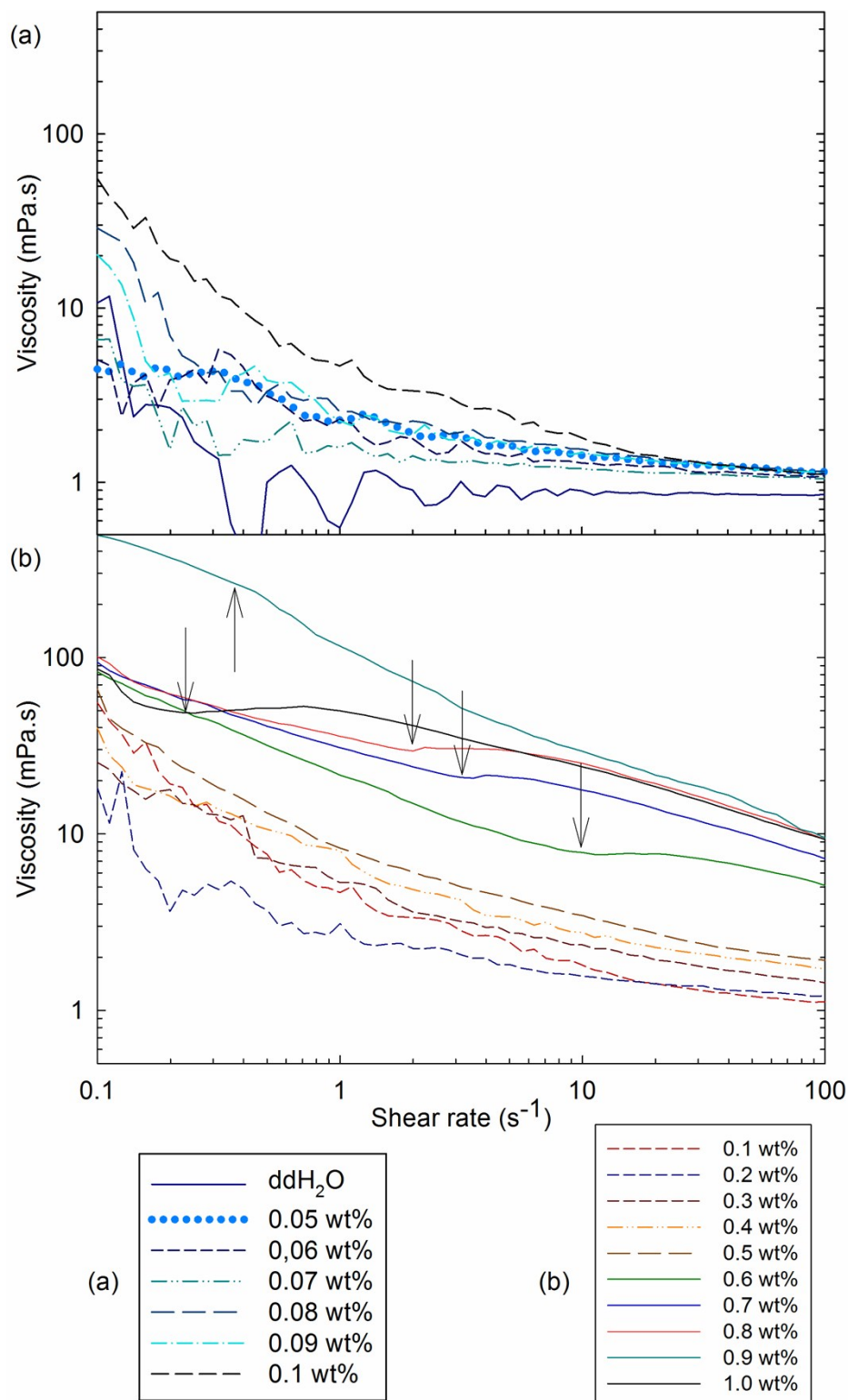


Figure S2. Viscosity measurements for the 2NapFF solution phase. (a) Subset of results for ddH₂O and concentrations between 0.05 and 0.1 wt%; (b) Subset of results for concentrations between 0.1 and 1.0 wt% and ddH₂O. The arrows indicate the transition to faster relaxation processes and short periods of shear thickening in between the shear thinning regions.

The region from 0.6 to 1.0 wt% appears to be the interval where the worm-like micellar structures are strongly entangled with junction points. In this region, the worm-like micellar solutions have a similar behaviour to what was described for CTAB surfactant in the entangled worm-like micellar region.¹ At low shear rates, the sample first shows shear thinning behaviour. This is followed by a weak shear thickening behaviour, in a range that shifts to low shear rates with increasing concentration. This feature is reproducible. The shear thinning behaviour continues after this feature. These results suggest an increase in the relaxation time (τ_R), as shown in Fig. S3. The relaxation time can be assessed through the measurement of the break times from the viscosity as a function of shear rate² (i.e. when the viscosity starts to plateau) and plotted in Fig. S3 using Equation S1.

$$\tau_R \approx \frac{1}{\dot{\gamma}} \quad (\text{Eq. S1})$$

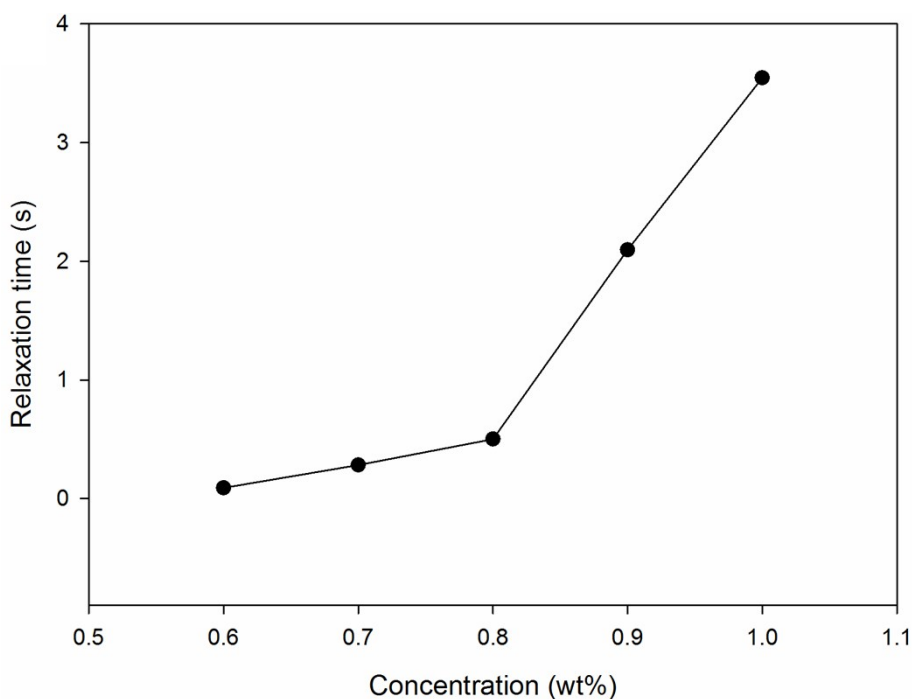


Figure S3. Relaxation time of the 2NapFF solution phase as a function of concentration obtained from the viscosity plateau regions.

From these measurements, we can see that there is an increase in relaxation time with an increase of concentration until 0.8 wt%. Above this concentration, the relaxation time increases dramatically, suggesting another order of self-assembly is occurring in the system. The concentration dependence of the phase appears to have a phase transition at 0.9 wt% and 0.1 wt% due to an increased viscosity at low shear rates, suggesting that there may be two phases at these concentrations. The 0.9 wt% transition and increase in relaxation time could be associated with lateral packing of the worm-like micelles, sometimes referred to as bundling, which causes the micelles to relax more slowly

because the bundling adds further relaxation modes to the network.² From 0.1 – 0.2 wt% to 0.5 wt% the viscosity at high shear rates increases with increasing concentration, suggesting that there is an increase in the number of worm-like micelles, similar to a CTAB surfactant system.¹

At concentrations between 0.6 wt% and 0.08 wt%, the viscosity suggests that there are worm-like micelles, however they might not be able to entangle to the same degree to produce the relaxation modes discussed above or the sensitivity of the rheometer does not allow us to identify these features. Below 0.08 wt%, the rheometer is near the torque limits and the gelator samples have a viscosity near the ddH₂O (Fig. S2), therefore these measurements are not sufficient to interpret the results at these low concentrations.

1.3 Frequency Sweeps

A full rheological characterization of the 2NapFF micellar solutions was conducted with frequency-sweep, strain-sweep and triple oscillation recovery measurements (Figures S4 and S5).

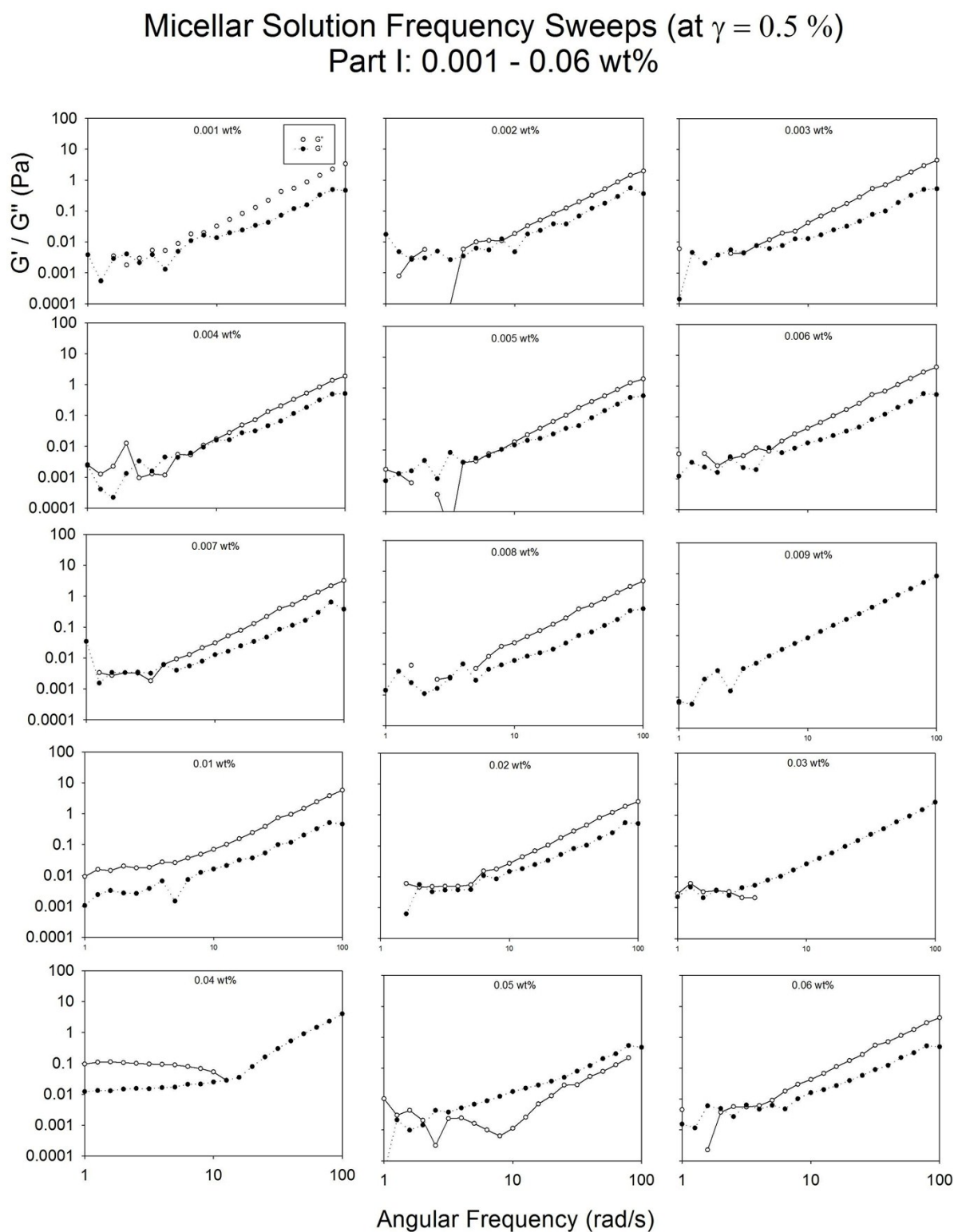


Figure S4. Frequency Sweeps of solutions of 2NapFF from 0.001 wt% up to 0.06 wt% at pH 10.5. In all cases, the closed symbols represent G' and the open symbols refer to G'' .

Micellar Solution Frequency Sweeps (at $\gamma = 0.5\%$) Part II: 0.07 - 1.0 wt%

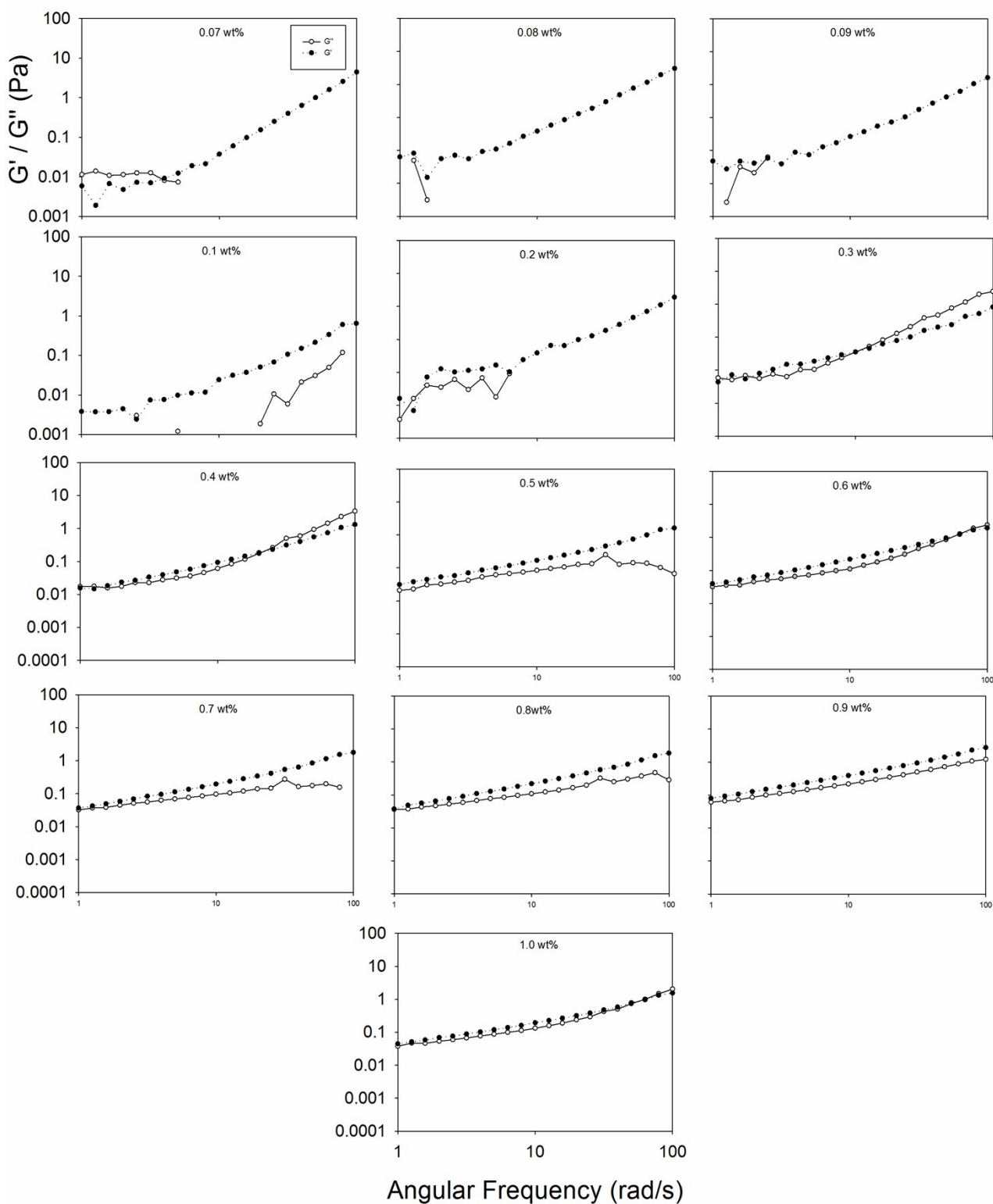


Figure S5. Frequency Sweeps of solutions of 2NapFF from 0.07 wt% up to 1.0 wt% at pH 10.5. In all cases, the closed symbols represent G' and the open symbols refer to G'' .

1.3.1 Analysis of Solution Frequency Sweeps

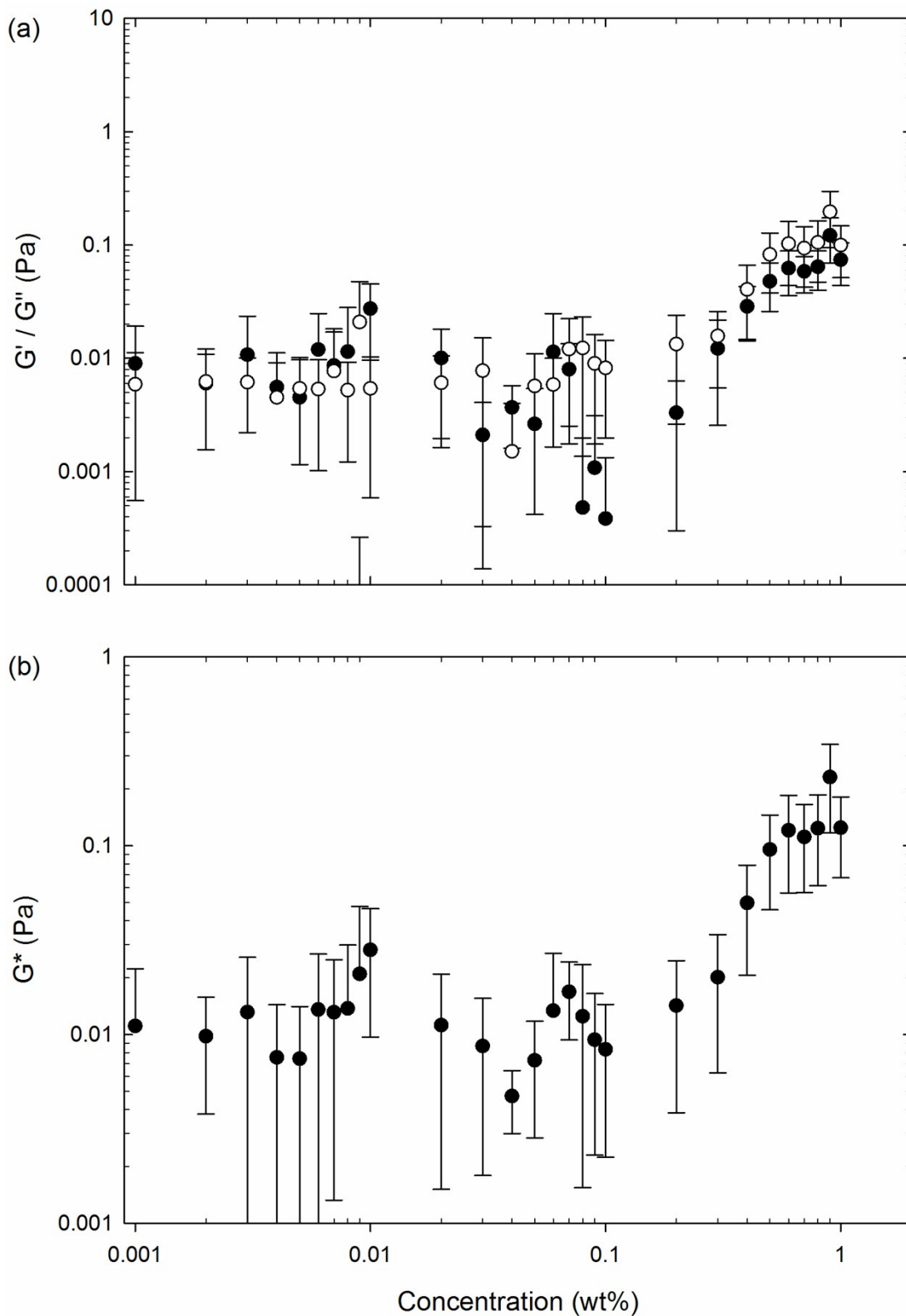


Figure S6. Summary of frequency sweeps analysis of solutions of 2NapFF from 0.001 wt% up to 1.0 wt% at pH 10.5 with $\gamma = 0.5\%$. Readings of absolute values were taken from the plateau region of the solution strain sweep plots. Shear modulus (G' , closed symbols) and Loss modulus (G'' , open symbols) are plotted against concentration (a) and the corresponding complex modulus (G^*) is plotted against concentration (b).

1.4 Strain Sweeps

Micellar Solution Strain Sweeps (at $\delta = 10$ rad/s) Part I: 0.001 - 0.06 wt%

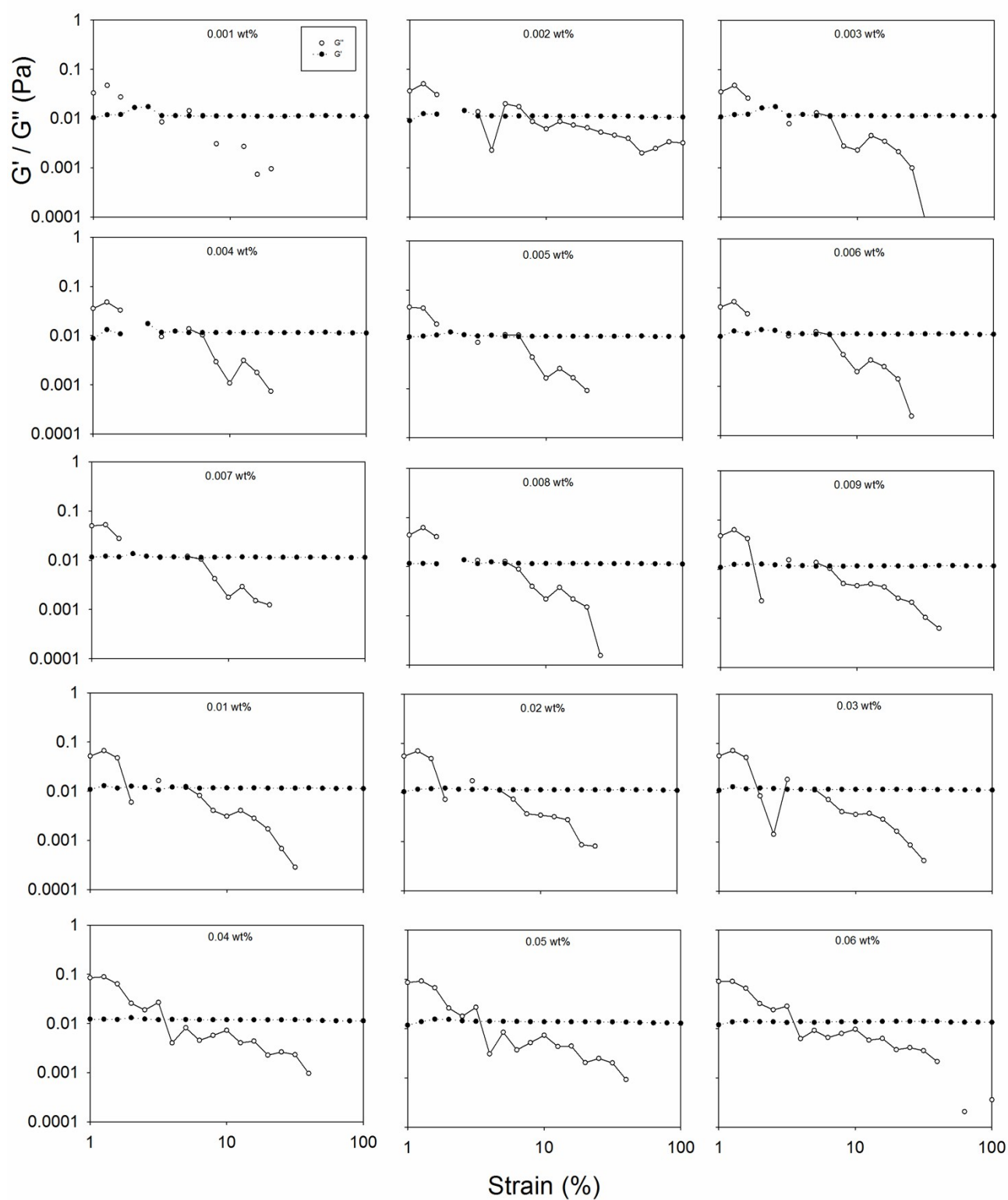


Figure S7. Strain Sweeps of solutions of 2NapFF from 0.001 wt% up to 0.06 wt% at pH 10.5. In all cases, the closed symbols represent G' and the open symbols refer to G'' .

Micellar Solution Strain Sweeps (at $\delta = 10$ rad/s) Part II: 0.07 - 1.0 wt%

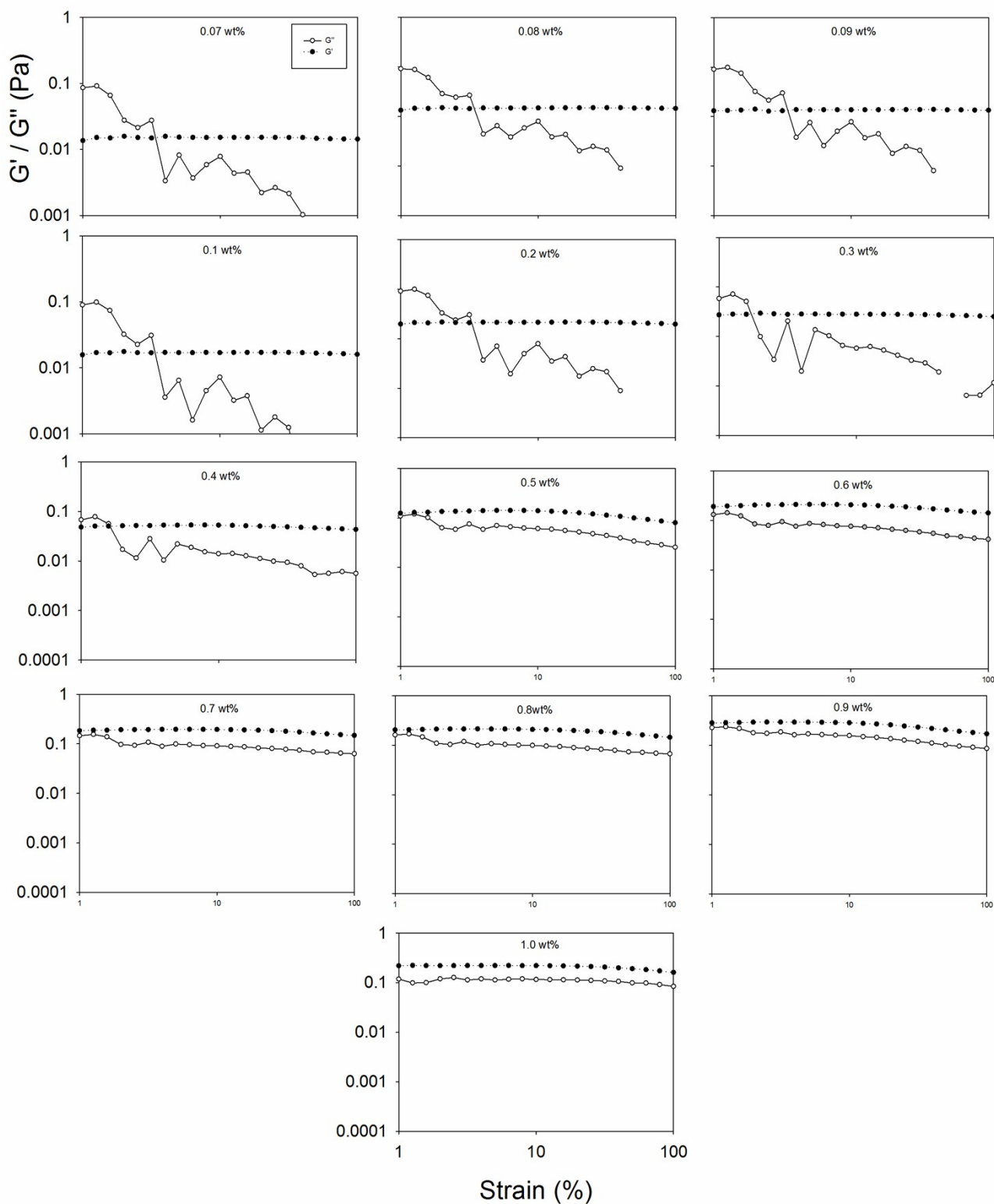


Figure S8. Strain Sweeps of solutions of 2NapFF from 0.07 wt% up to 1.0 wt% at pH 10.5. In all cases, the closed symbols represent G' and the open symbols refer to G'' .

1.4.1 Analysis of Solution Strain Sweeps

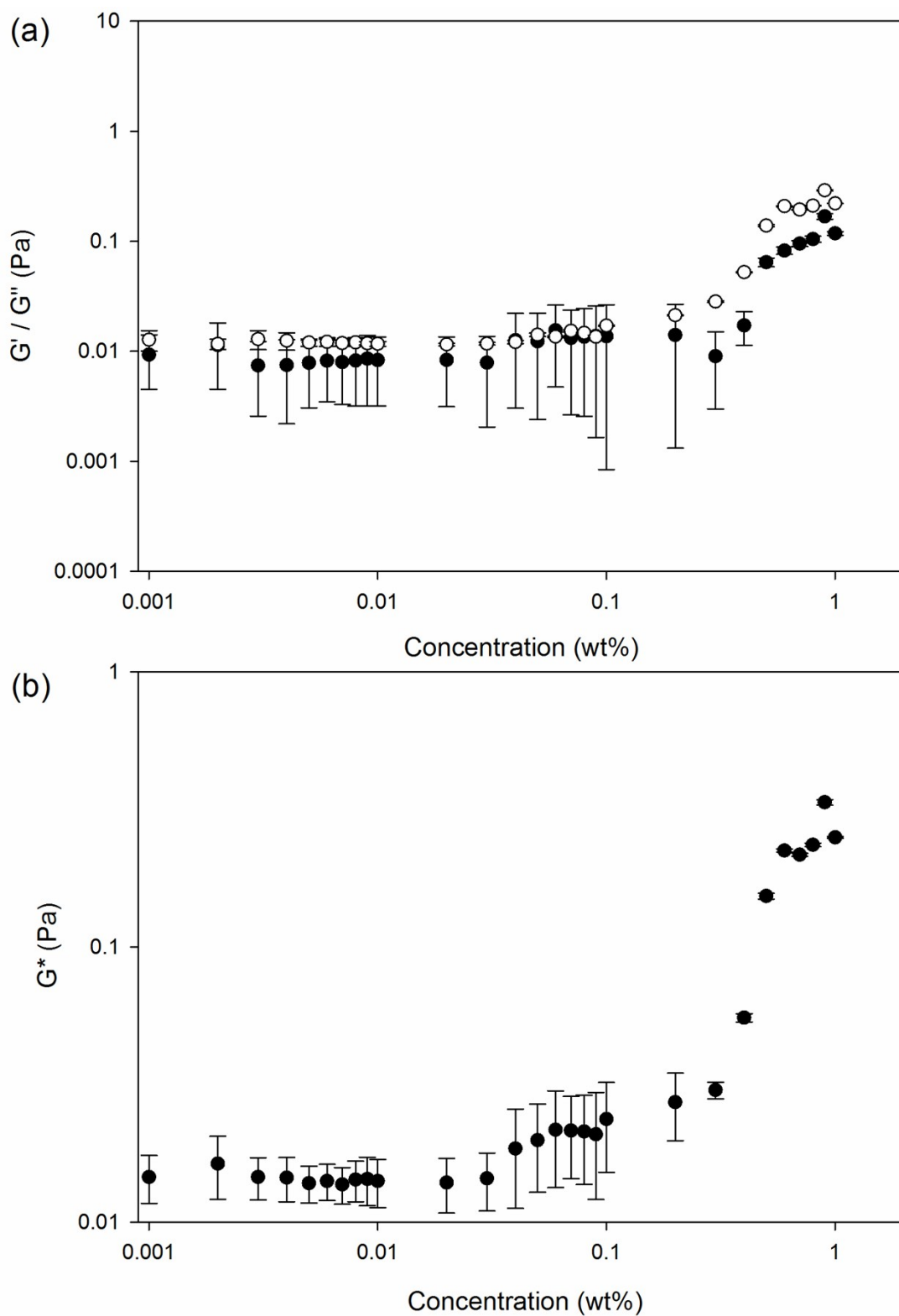


Figure S9. Strain sweeps analysis of solutions of 2NapFF from 0.001 wt% up to 1.0 wt% at pH 10.5 with $\delta = 10$ rad/s. Readings of absolute values were taken from the plateau region of the solution strain sweep plots. In all cases, the closed symbols represent G' and the open symbols refer to G'' .

2. Properties of the 2NapFF Ca-hydrogels

2.1 Frequency sweeps

Ca-Hydrogel Phase Frequency Sweeps (at $\gamma = 0.5\%$) Part I: 0.001 - 0.06 wt%

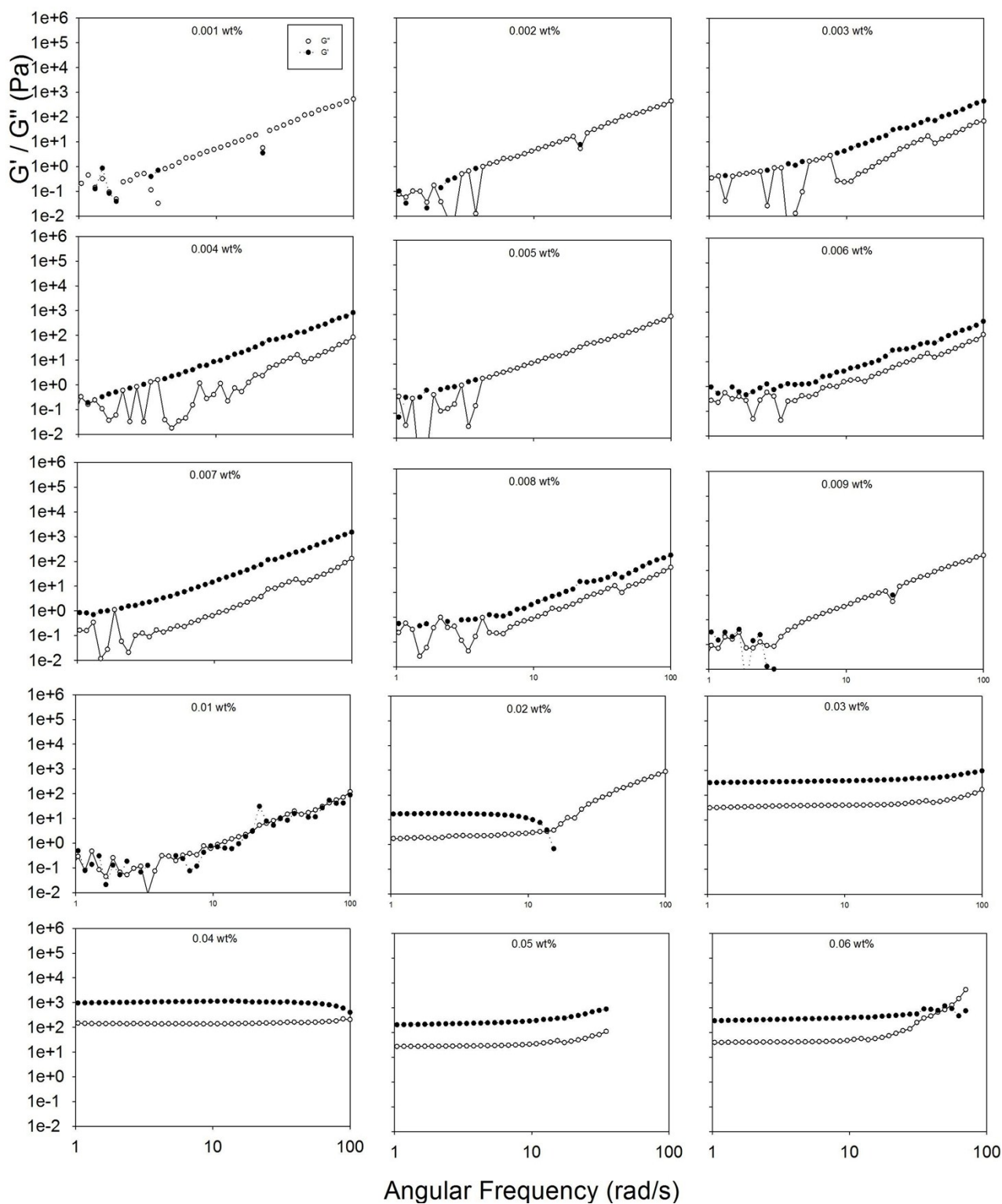


Figure S10. Frequency sweeps of Ca-hydrogels of 2NapFF from 0.001 wt% up to 0.06 wt% at pH 10.5. In all cases, the closed symbols represent G' and the open symbols refer to G'' .

Ca-Hydrogel Phase Frequency Sweeps (at $\gamma = 0.5\%$) Part I: 0.07 - 1.0 wt%

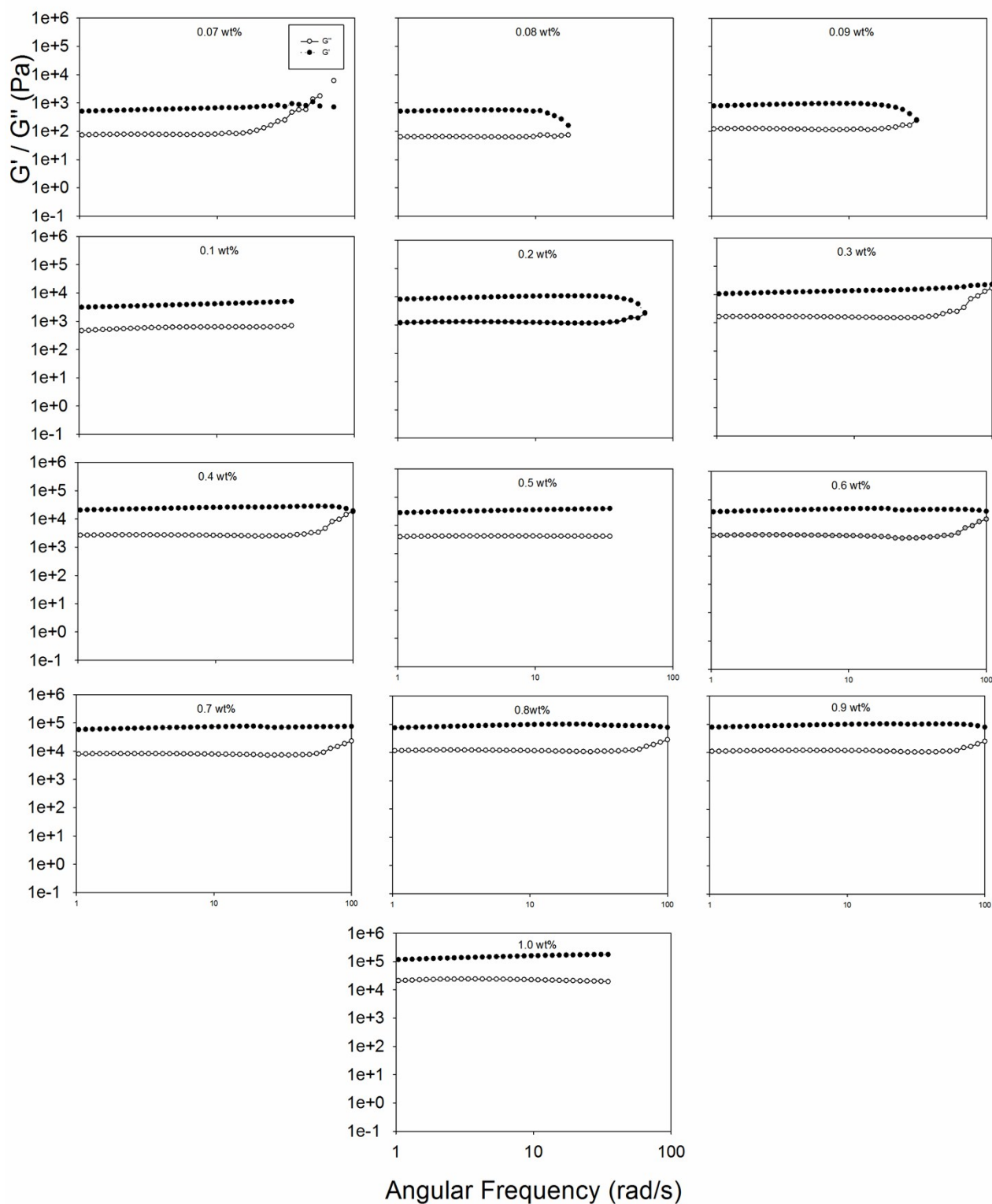


Figure S11. Frequency sweeps of Ca-hydrogels of 2NapFF from 0.07 wt% up to 1.0 wt% at pH 10.5. In all cases, the closed symbols represent G' and the open symbols refer to G'' .

2.1.1 Analysis of Hydrogel Frequency Sweeps

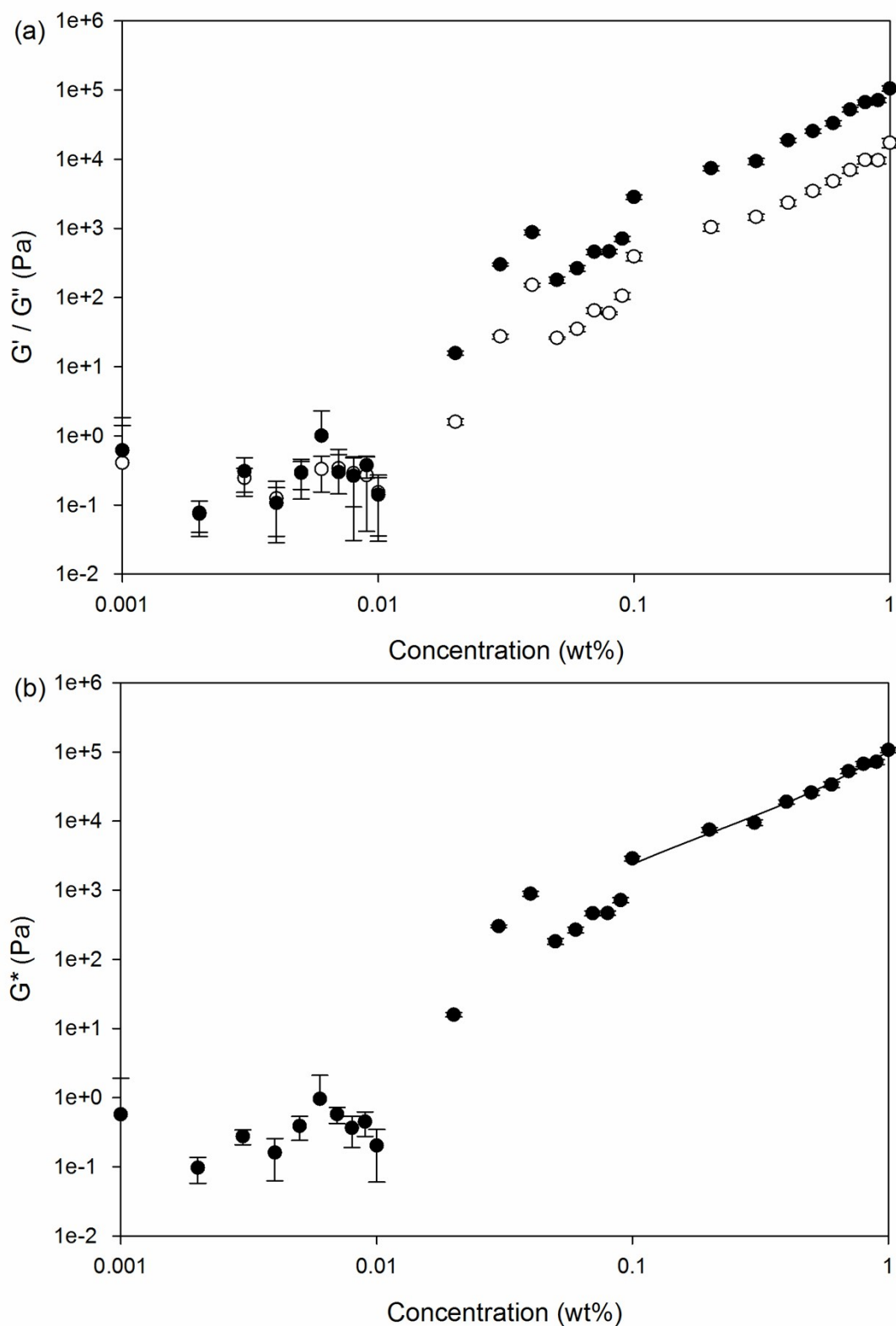


Figure S12. Summary of frequency sweeps analysis of Ca-hydrogels of 2NapFF from 0.001 wt% up to 1.0 wt% at pH 10.5, with $\gamma = 0.5$ %. Readings of absolute values were taken from the plateau region of the solution strain sweep plots. A concentration dependent exponential fit is obtained in the region from 0.1 to 1 wt% with a $R^2 > 98$ %. In all cases, the closed symbols represent G' and the open symbols refer to G'' .

2.2 Strain sweeps

Ca-hydrogel phase Strain Sweeps (at $\delta = 10$ rad/s) Part I: 0.001 - 0.06 wt%

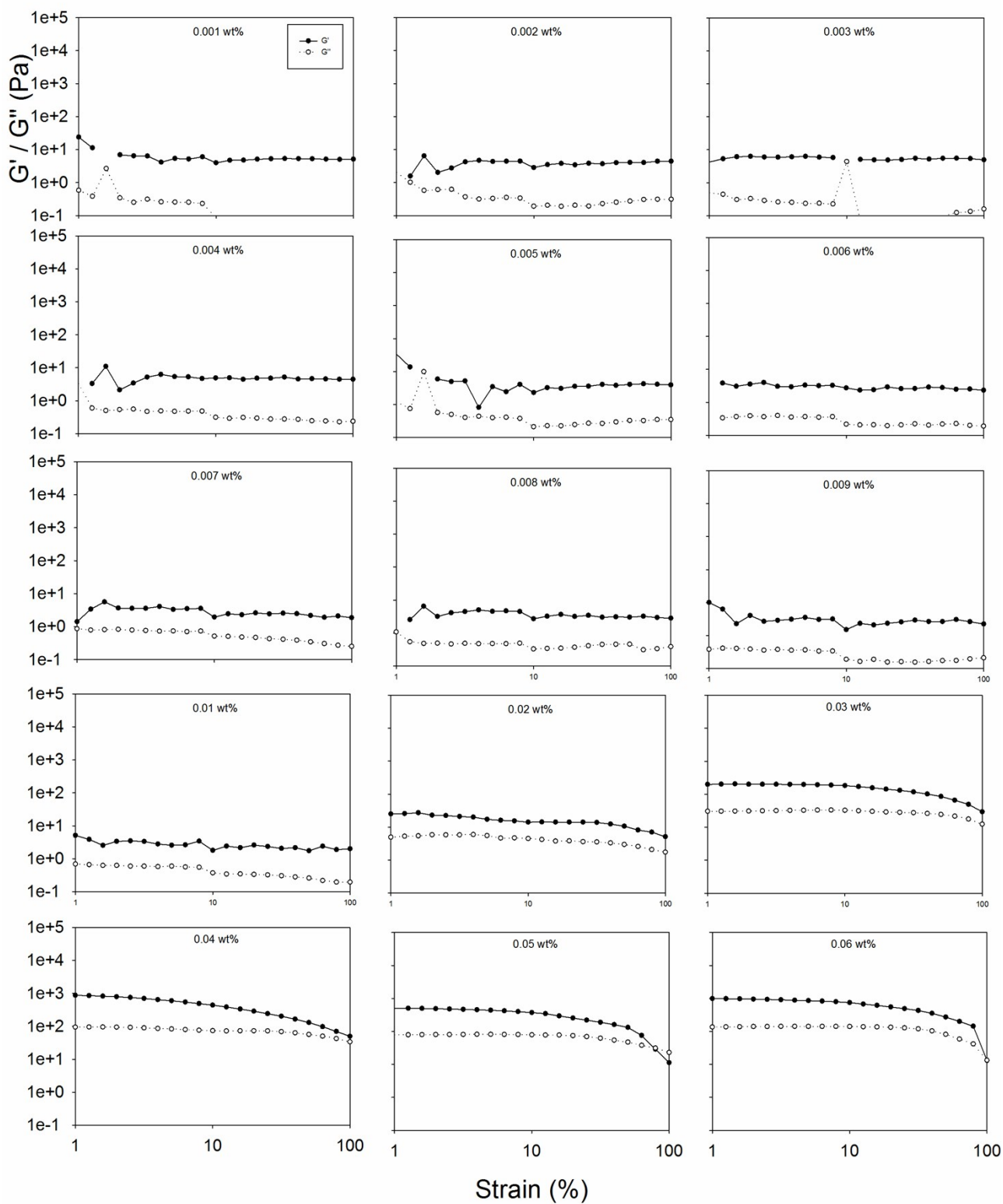


Figure S13. Strain sweeps of Ca-hydrogels of 2NapFF from 0.001 wt% up to 0.06 wt% at pH 10.5. In all cases, the closed symbols represent G' and the open symbols refer to G'' .

Ca-hydrogel phase Strain Sweeps (at $\delta = 10$ rad/s) Part II: 0.07 - 1.0 wt%

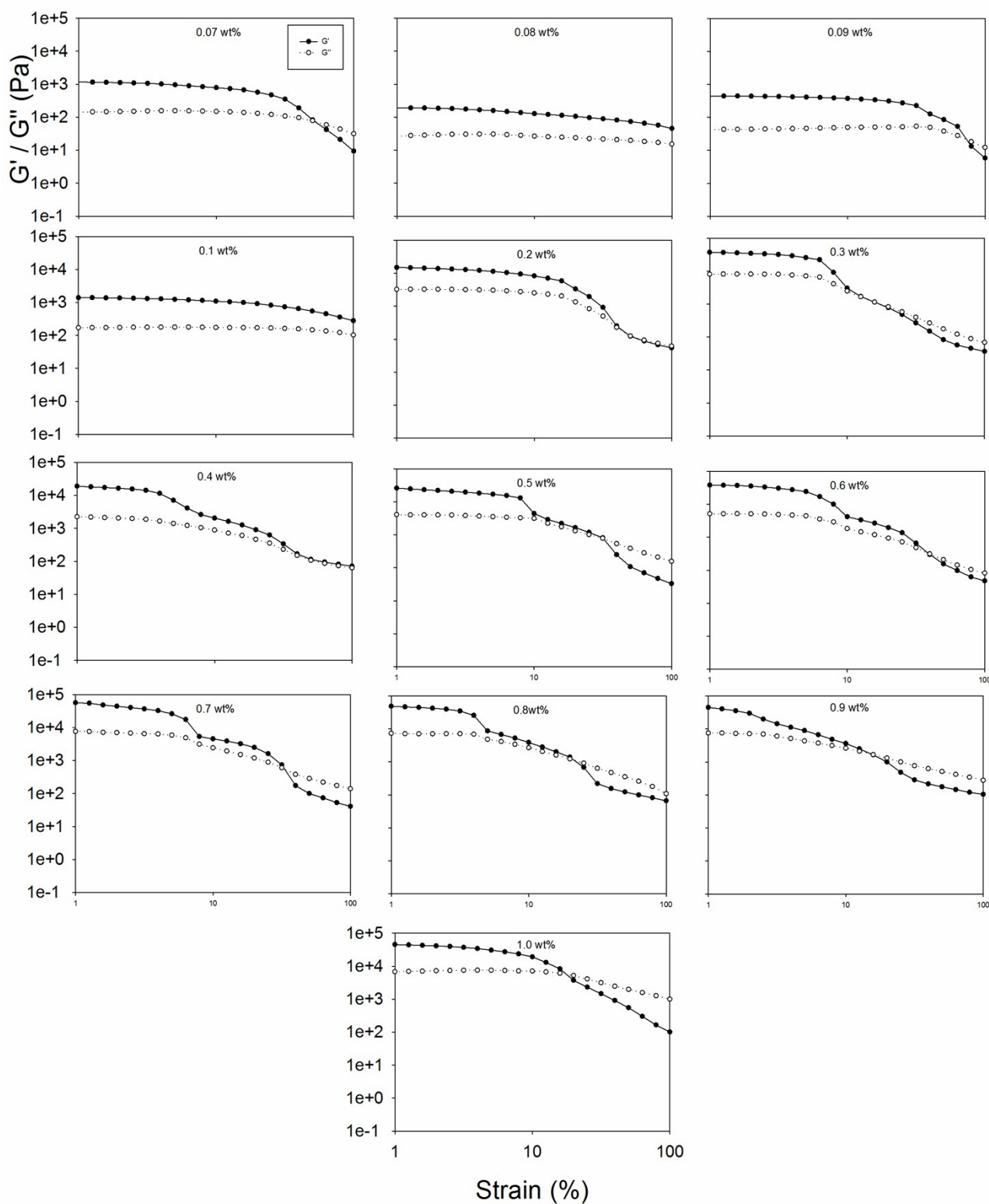


Figure S14. Strain sweeps of Ca-hydrogels of 2NapFF from 0.07 wt% up to 1.0 wt% at pH 10.5. In all cases, the closed symbols represent G' and the open symbols refer to G'' .

2.2.1 Analysis of Hydrogel Strain Sweeps

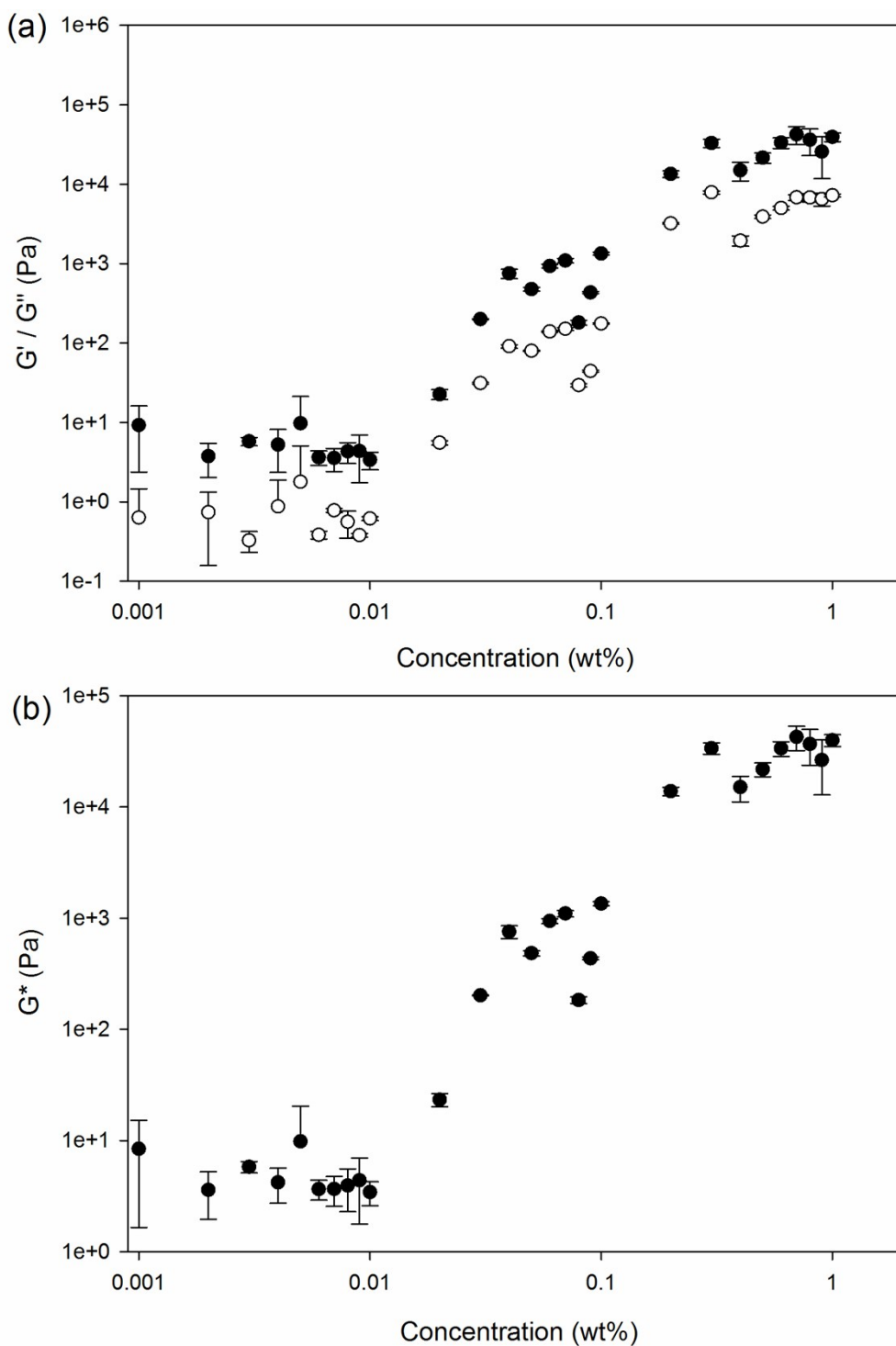


Figure S15. Summary of strain sweeps analysis of Ca-Hydrogels of 2NapFF from 0.001 wt% up to 1.0 wt% at pH 10.5, with $\delta = 10$ rad/s. Readings of absolute values were taken from the plateau region of the solution strain sweep plots. In all cases, the closed symbols represent G' and the open symbols refer to G'' .

2.3 Recovery tests of the Ca-hydrogels

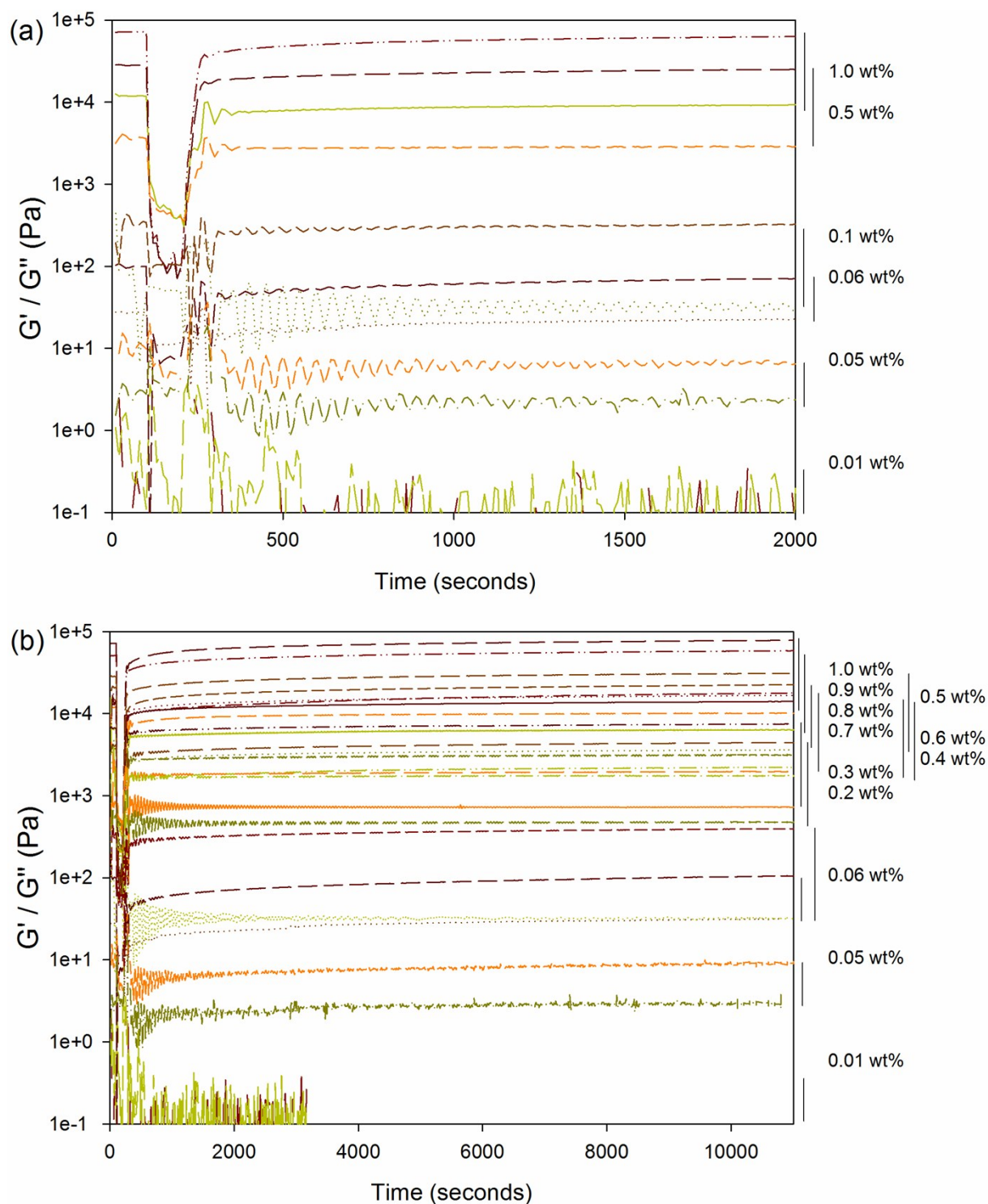


Figure S16. Triple oscillation recovery tests (as described above, section 1.5) for 2NapFF Ca^{2+} hydrogels formed with 2:1 Ca^{2+} :gelator ratio across a range of concentrations from 0.01 to 1.0 wt%. On the right side of the graph a schematic legend shows a line guide between the G' (top side of all lines) and G'' (bottom side of all lines) for each concentration. The recovery results are plotted for a selected number of samples at early time points, the first 33 minutes (a) and over a longer period of time, 3 hours (b). All hydrogels show full recovery (0.05 wt% and above).

2.3.1 Analysis of Hydrogel Recovery tests

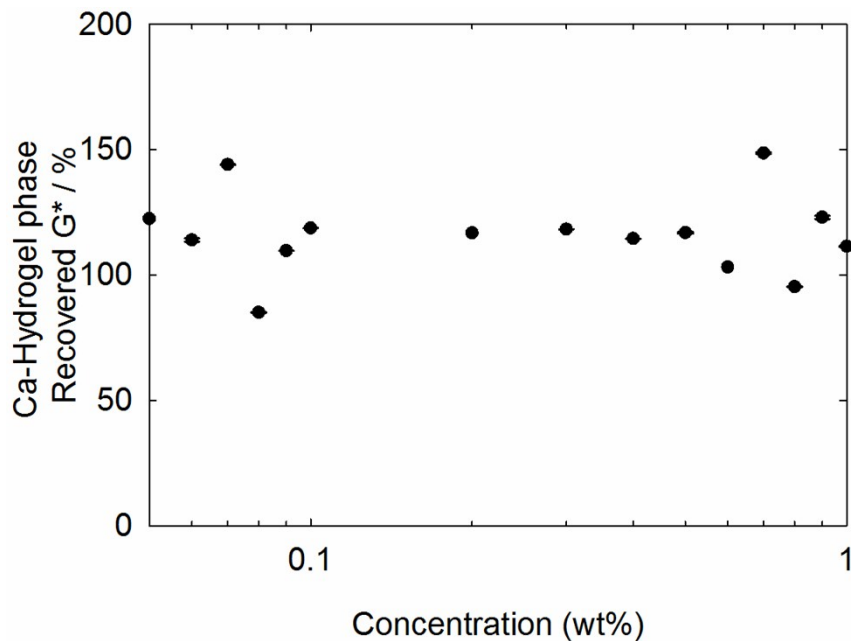


Figure S17. Recovery percentage for the G^* of the Ca-hydrogel phase at 20.000 s (or at plateau) after cessation of high strain (100%), when compared with the starting G^* at the low shear (0.5 %) initial measurement. The recovery protocol is described in section 1.5.

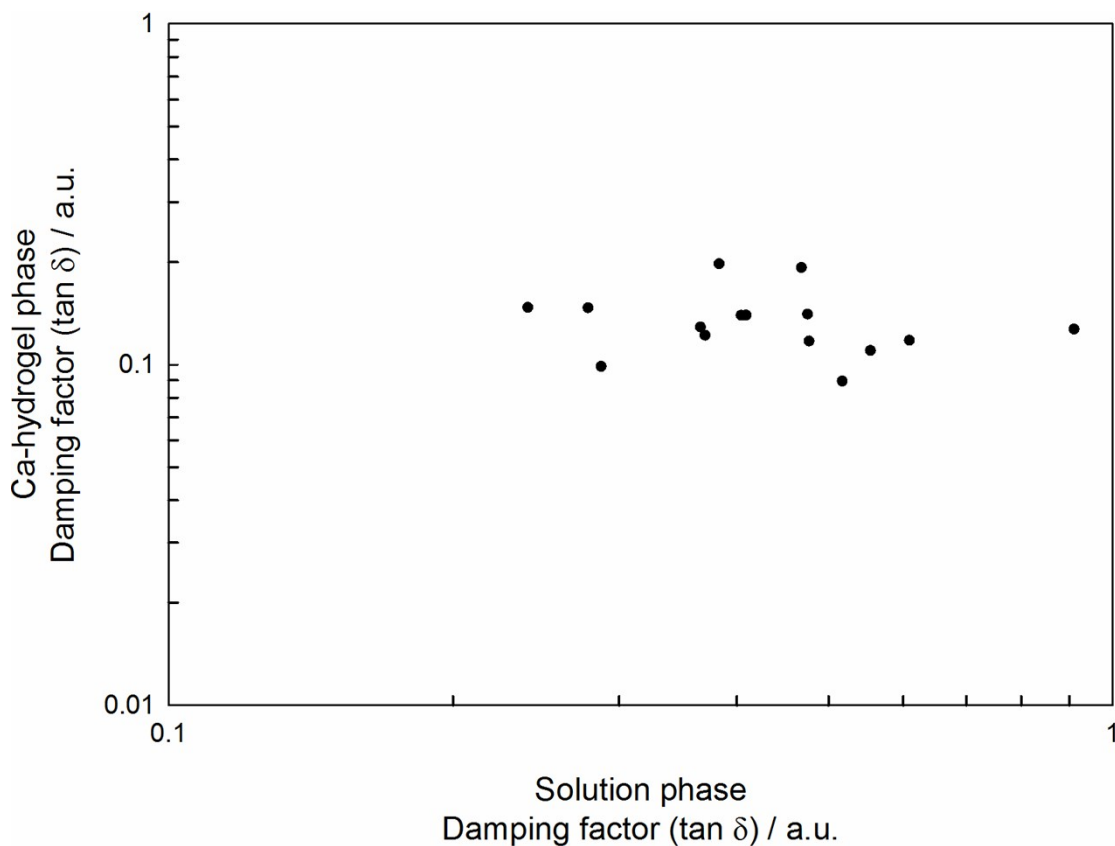


Figure S18 – Analysis of the correlation of solution and hydrogel phase by the damping factor, $\tan \delta$.

3. FTIR of 2NapFF Solutions and Ca-Hydrogels

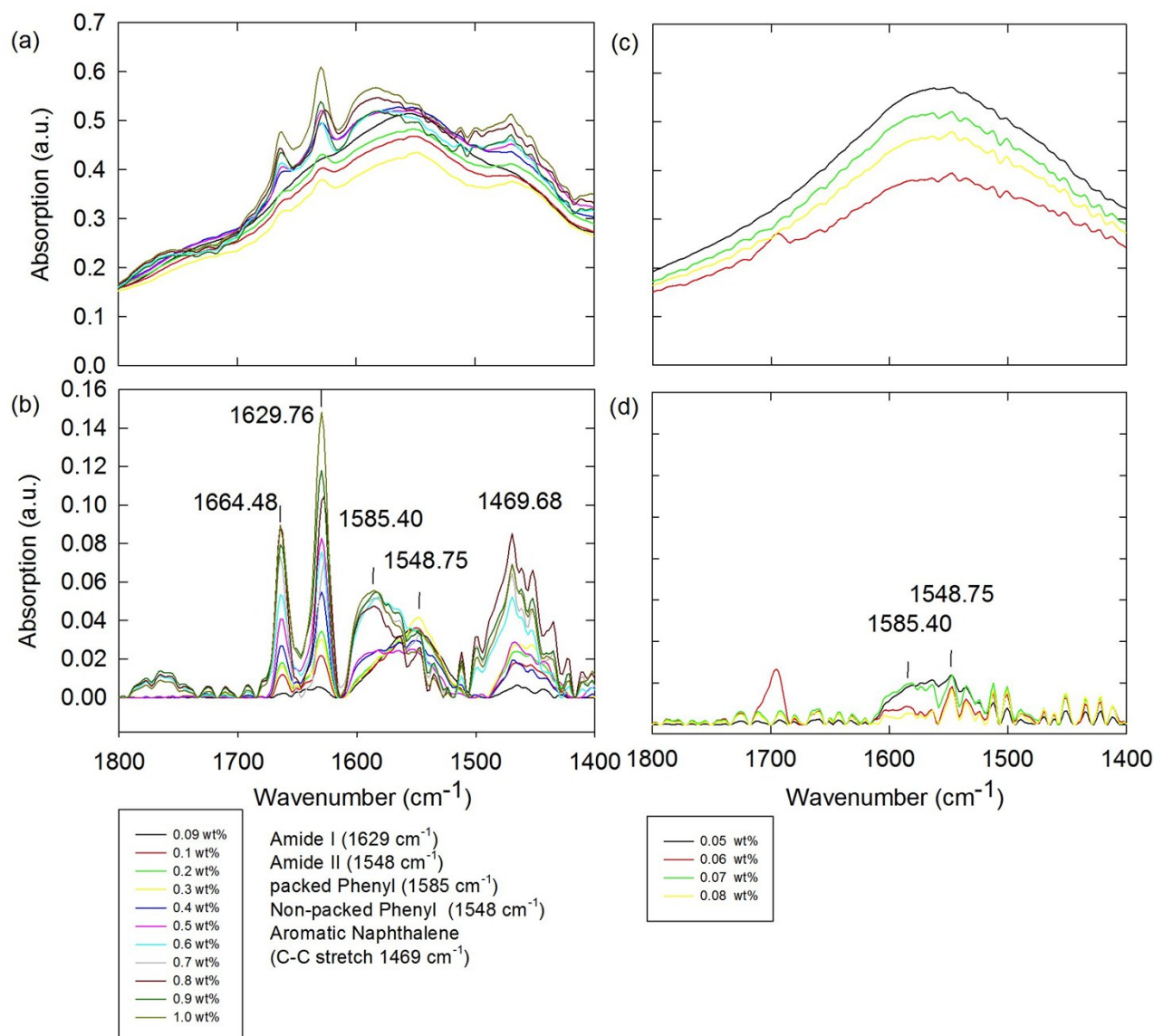


Figure S19. FTIR of 2NapFF Micellar Solutions in a liquid-cell system as a function of concentration at pD 11.5 ± 0.5 in D_2O for high ((a) and (b)) and low ((c) and (d)) concentration region with air background subtracted ((a) and (c)) and with baseline correction with baseline concave rubberband model ((b) and (d)). In (a) and (c), the spectra were collected with only the air and CaF_2 windows as background absorption, thus a broad peak with a maximum at 1550 cm^{-1} appears due to residual water in this region. In (b) and (d), a baseline correction option in OPUS 7.0 software (baseline concave rubberband correction method) was used to suppress the broad water peak influence in the spectra.

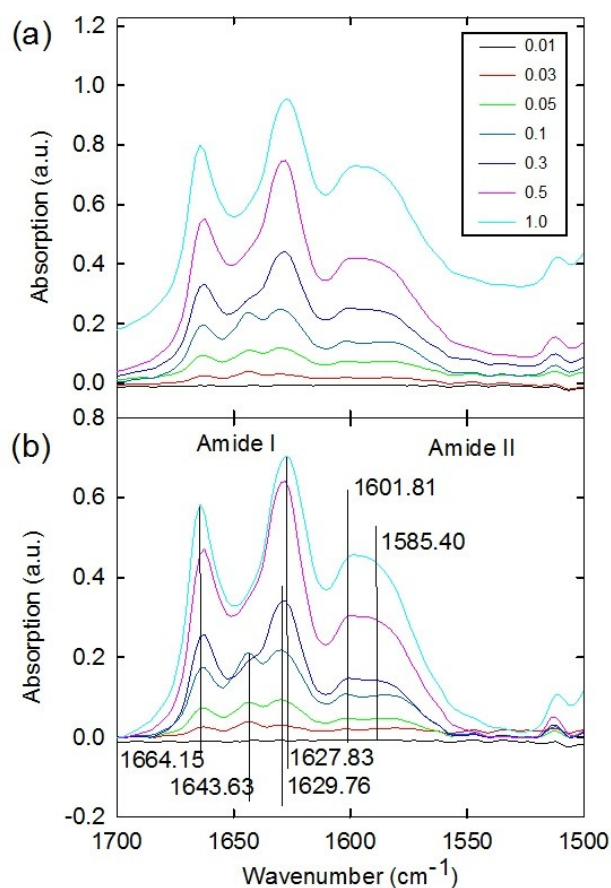


Figure S20. FTIR spectra of (a) 2NapFF Ca-hydrogels at high pD 11.5 ± 0.5 without the baseline correction and (b) with the baseline correction option in OPUS 7.0 software (baseline concave rubberband correction method).

4. Microscopy of the 2NapFF Ca-hydrogels

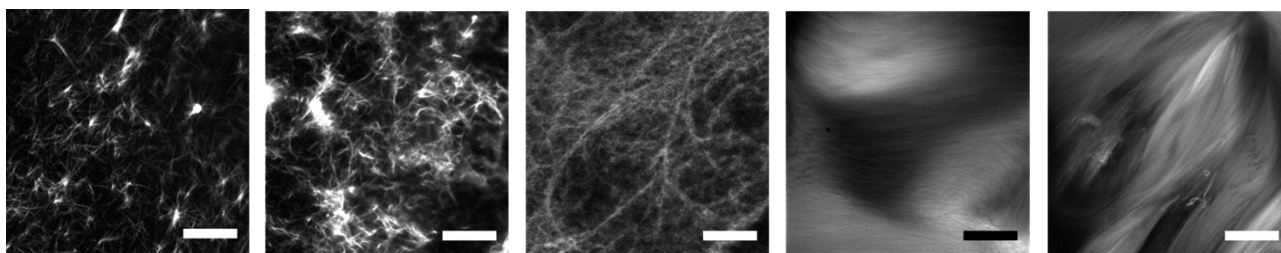


Figure S21. Confocal Micrographs of aqueous 2NapFF calcium nitrate hydrogels at concentrations of 0.05, 0.1, 0.3, 0.5 and 1.0 wt% (left to right), with 0.0002 M Nile Blue staining, after 24 hour incubation at RT ($22\text{ }^{\circ}\text{C}$) the solutions were gelled with 0.02 M $\text{Ca}(\text{NO}_3)_2$. Observations were conducted after 4 days of incubation in sealed confocal glass dishes. All scale bars are 20 μm .

5. SEM images of the Ca-hydrogels

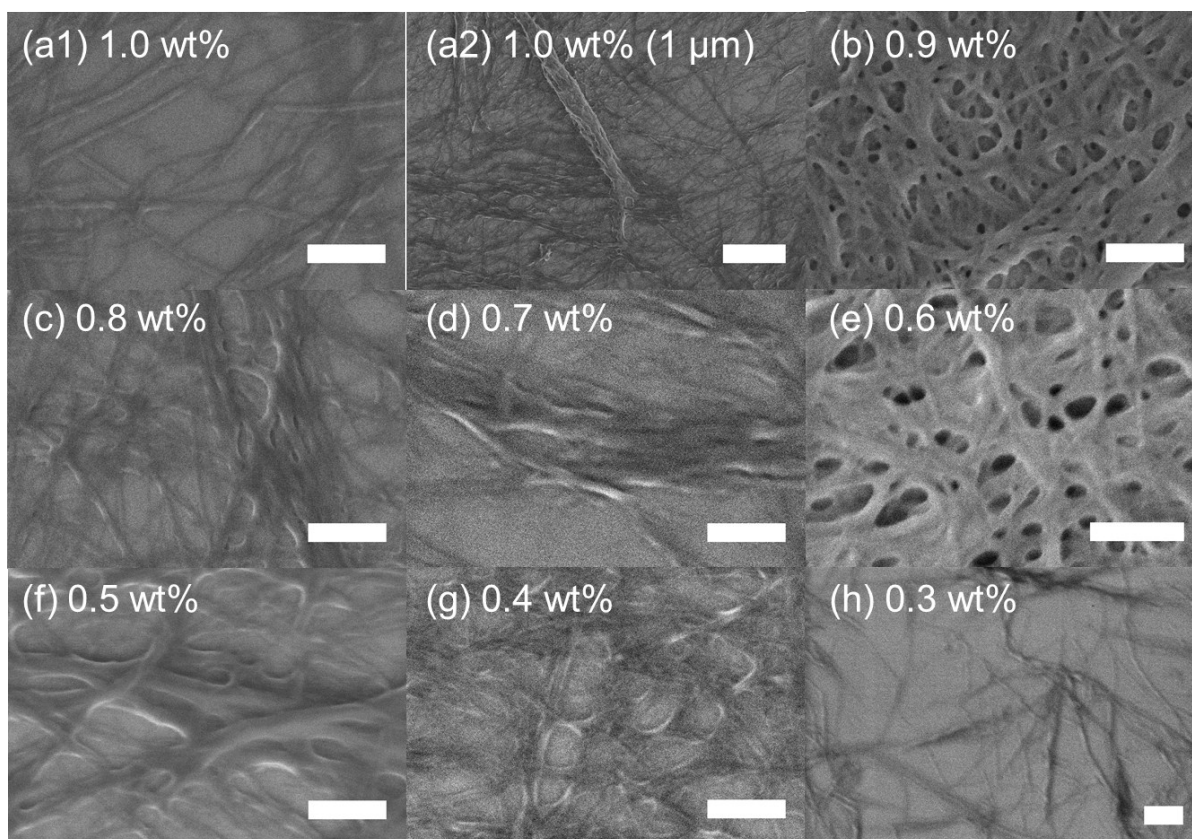


Fig. S22. 2NapFF Ca-hydrogels imaged by SEM with no coating at concentrations of 1.0 wt% (a1), 1.0 wt% (a2, 1 μm), 0.9 wt% (b), 0.8 wt% (c), 0.7 wt% (d), 0.6 wt% (e), 0.5 wt% (f), 0.4 wt% (g) and 0.3 wt% (h). Image (a2) shows the typical presence of larger bundles observed with a lower magnification. The scale bars represent 250 nm, except (a2) image has a 1 μm scale bar.

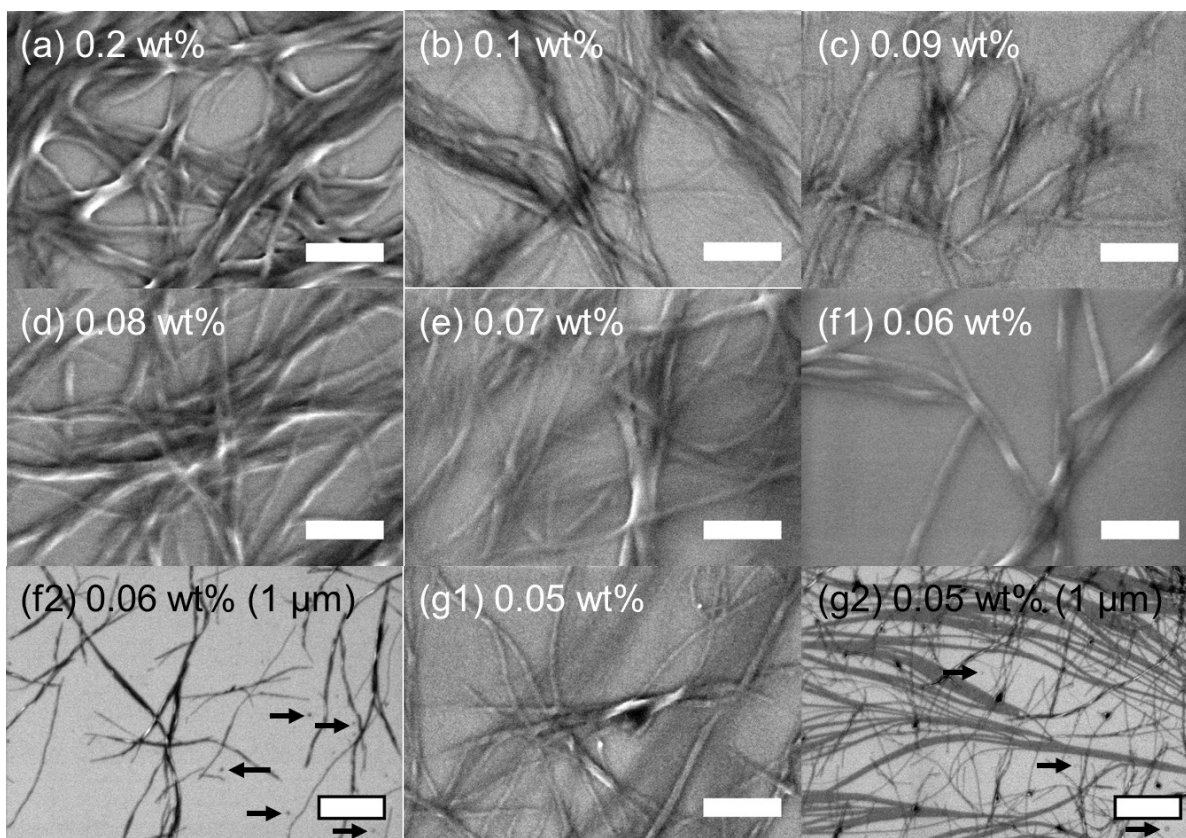


Fig. S23. 2NapFF Ca-hydrogels imaged by SEM with no coating at concentrations of 0.2 wt% (a), 0.1 wt% (b), 0.09 wt% (c), 0.08 wt% (d), 0.07 wt% (e), 0.06 wt% (f1), 0.06 wt% (f2, 1 μm), 0.05 wt% (g1) and 0.05 wt% (g2, 1 μm). Image (f2) and (g2) shows the typical presence of spherical aggregates observed with a lower magnification. The scale bars represent 250 nm, except (f2) and (g2) images have 1 μm scale bars.

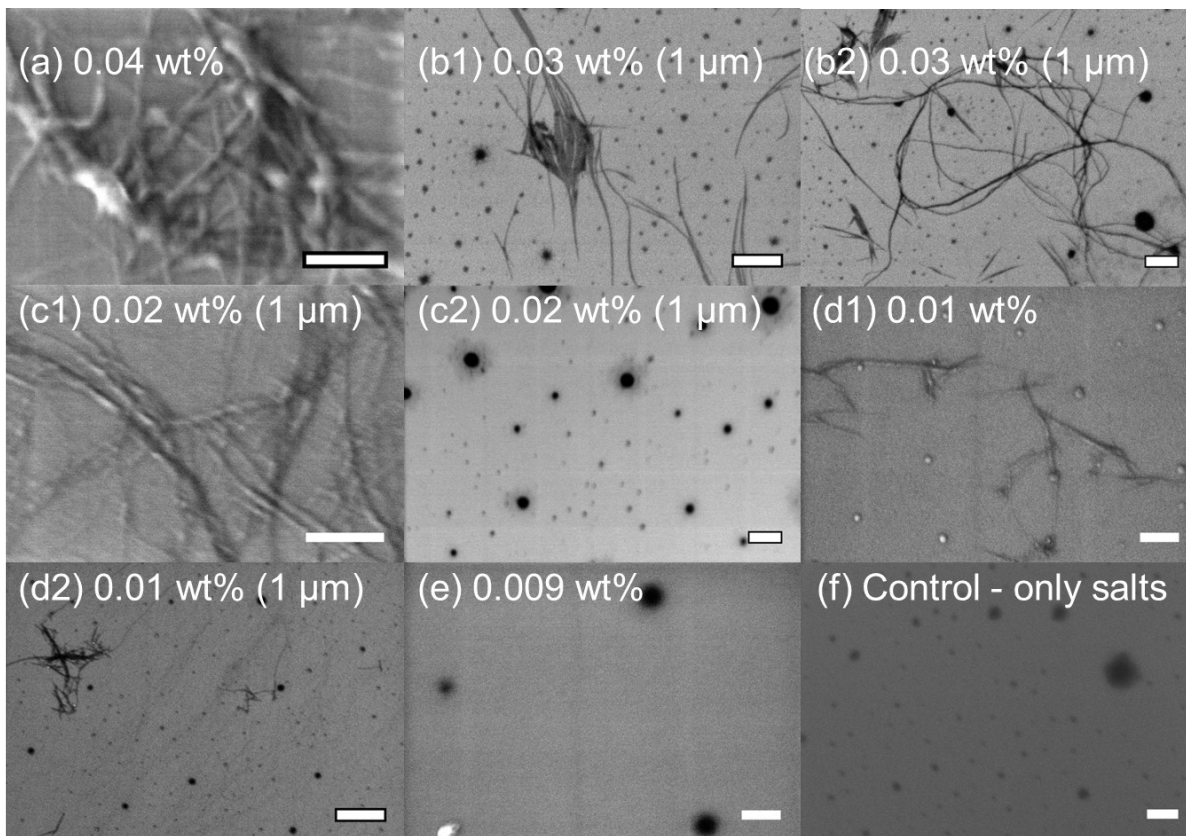


Fig. S24. 2NapFF Ca-hydrogels imaged by SEM with no coating at concentrations of 0.04 wt% (a), 0.03 wt% (b1), 0.03 wt% (b2, 1 μm), 0.02 wt% (c1), 0.02 wt% (c2, 1 μm), 0.01 wt% (d1), 0.01 wt% (d2, 1 μm), 0.009 wt% (e) and control sample prepared with the salt conditions used in the 0.03 wt% sample (f). The scale bars represent 250 nm, except (b1), (b2), (c1), (c2) and (d2) images have 1 μm scale bars.

6. Small angle neutron scattering (SANS) of 2NapFF Solutions and Ca-hydrogels

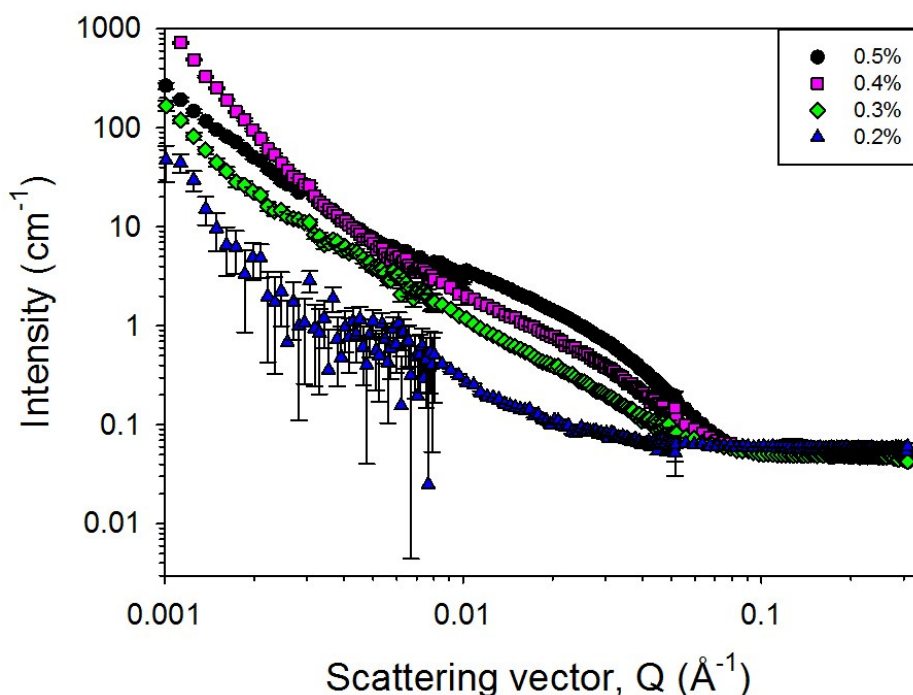


Figure S25. SANS profiles for 0.2 to 0.5 wt% solutions (unfitted) without solvent background subtraction (only empty cell subtracted) to avoid over-subtraction from the weakest data set. D₂O has flat scattering at around 0.05 cm⁻¹. The feature relating to the worm-like micelles at around 0.02 Å⁻¹ develops with increasing concentration.

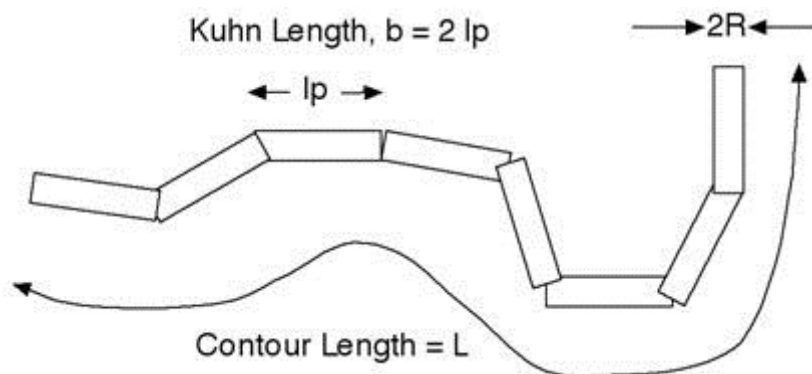


Figure S26. Schematic showing the parameters associated with the dimensions of the worm-like chain in the Kratky-Porod flexible cylinder model within SasView.³

Two models were used to fit the SANS data, each combines a power law with the scattering form factor, $P(Q)$, for a different type of cylindrical scatterer (C); a hollow rod⁴ (H) and the Kratky-Porod (KP) flexible cylinder,^{5,6} Equation S2.

$$I = SF_O (SF_{PL} P(Q)_{PL} + SF_C P(Q)_C) + \text{Background} \quad (\text{Eqn S2})$$

The hollow cylinder form factor implemented by SasView uses the equation derived by Guinier⁷ and is radially averaged with the rods having no preferred orientation. The parameters to describe it are an outer shell radius, R , an inner core radius, R_{core} , and a length, L_H . The flexible cylinder model describes a worm-like chain of length, L , made from freely jointed units with a segment length, l_p , which is half of the Kuhn length fitting parameter and a cross-sectional radius, R (Fig. S23). The other parameters in both models include: an overall scale factor, SF_O , fixed at 1; a simple numerical scaling factor for the power law component of the model, SF_{PL} , related to the density of the network; a scale factor for the worm-like cylindrical component, SF_C , corresponding to the volume fraction of the cylinders (of the size described by the model); and a flat background to account for the incoherent background scattering from the sample.

We have previously fitted data using the Kholodenko-Dirac (KD) worm-like chain model⁸ and in the region we are working the differences between the KD worm and the KP worm, as applied by the flexible chain, are smaller than the uncertainties. The flexible chain model was used here for computational convenience, but both are designed to interpolate between the expected Q^{-1} dependence for the rod-like character of the cylindrical elements, the Q^{-2} associated with the cross-section of the cylinder and a limiting Q^{-4} associated with the globular nature over large distances.

A comparison between the model fit obtained from the customised hollow and flexible cylinder models are shown in Fig. S27. This demonstrates how the two different models are most appropriate for the two different types of data set; solution and gel as the alternative models are unsuccessful. The alternative models were also applied with a polydispersity included but for the solution data the flexible cylinder version could not capture the intensity of the fringe at high Q . While the addition of polydispersity allowed the hollow cylinder to fit the high Q region of the gel data it continued to deviate at low Q in the same way shown by the unsuccessful fit in S27b.

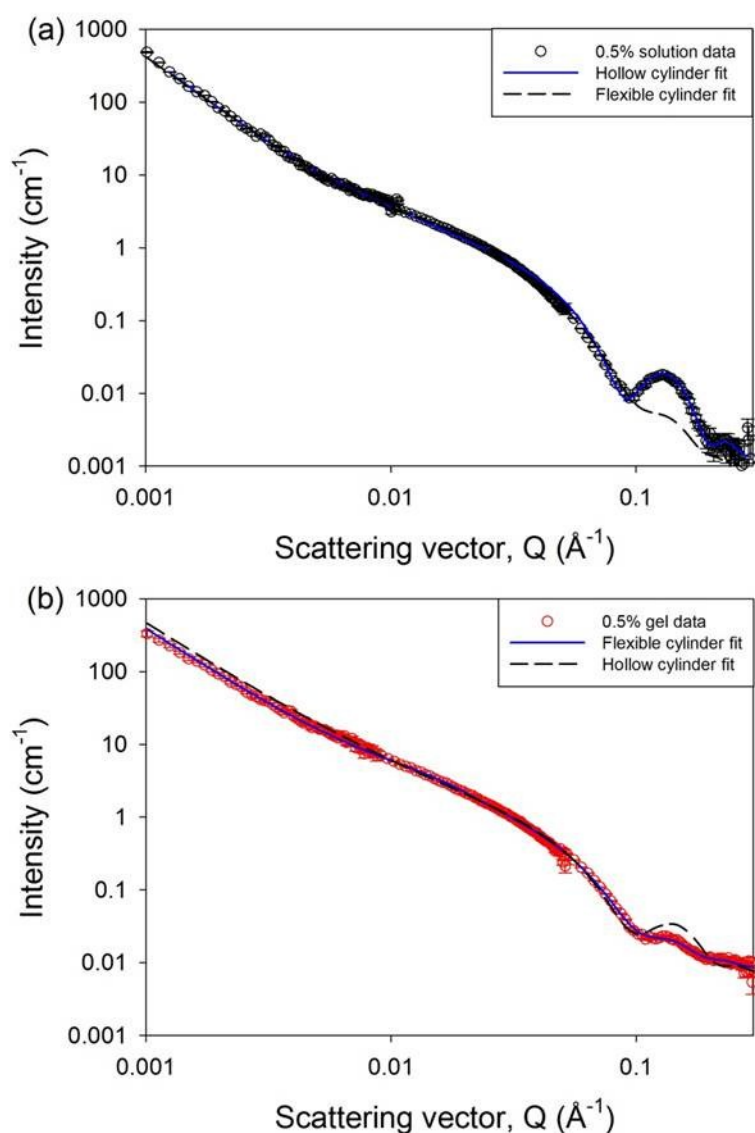


Figure S27. (a) 0.5 wt% solution with a comparison of the successful hollow cylinder fit with the unsuccessful flexible cylinder model fit and (b) the gel with its successful flexible cylinder fit compared to the unsuccessful hollow cylinder model fit. Both models included the power law term as described in the text.

When fitting, some conditions were imposed such as the Kuhn length had to be larger than $2R$, and less than the overall length. The scattering length densities (SLDs) of the cylinder, made from 2NapFF ($2.73 \times 10^{-6} \text{ \AA}^{-2}$), and the solvent, predominantly D_2O ($6.3 \times 10^{-6} \text{ \AA}^{-2}$), were fixed. The SLD for 2NapFF has been estimated from a structure calculation, however the model was tested with a range of SLD values ($\pm 1 \times 10^{-6} \text{ \AA}^{-2}$) and the only parameter that required adjustment to obtain an equally good fit was the SF_C , which we do not attempt to analyse for its absolute value, therefore our choice of SLD does not impact on comparison of SF_C values between data sets. Uncertainties were taken based on where the fit began to deviate from a visually good quality fit. All parameters for those successful fits in Figs S27 and S28 are provided in Table S1.

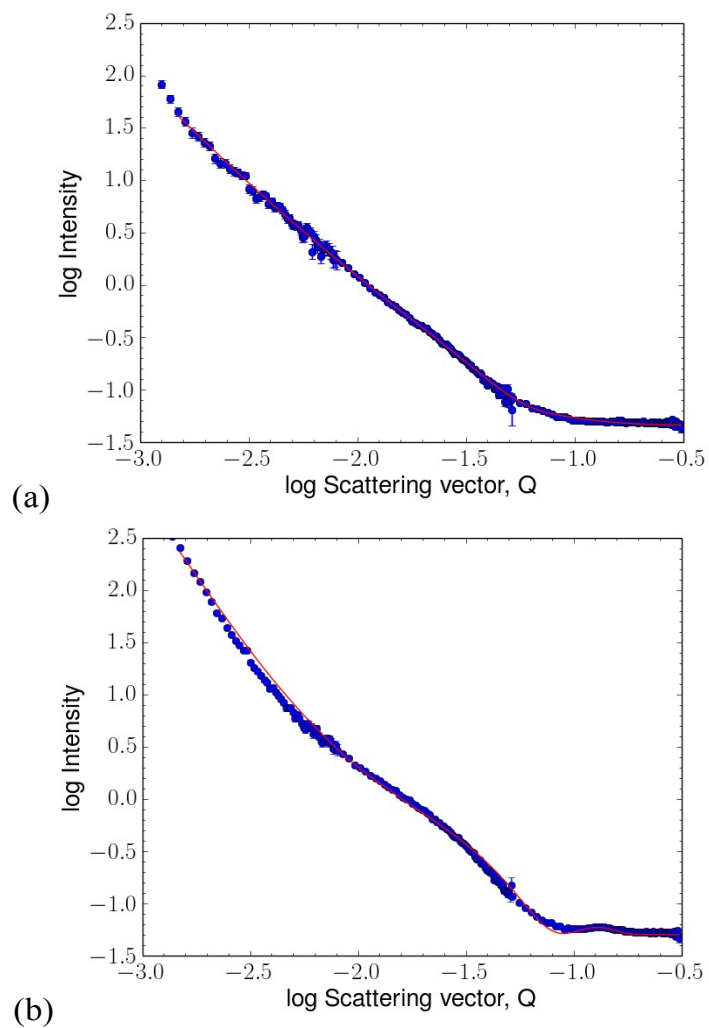


Figure S28. Model fits using the hollow cylinder combined with the power law for (a) the 0.3 wt% solution and (b) the 0.4 wt% solution.

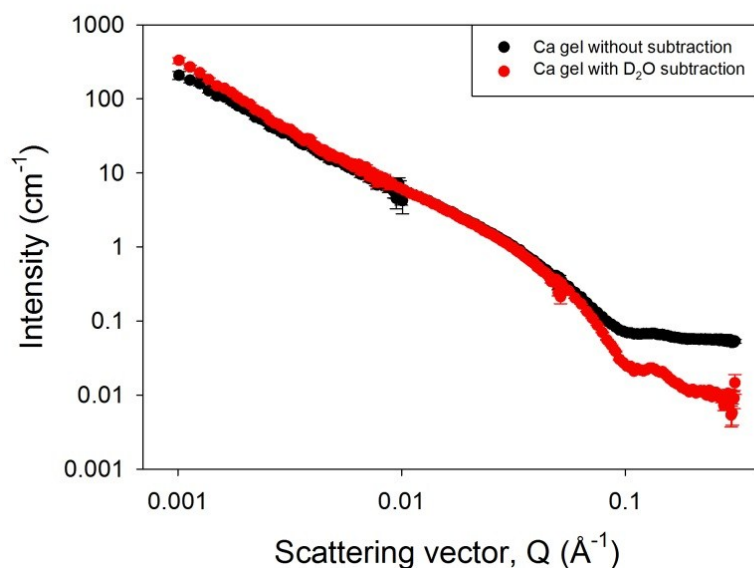


Figure S29. Normalised SANS data for the 0.5 wt% Ca gel with and without subtraction of normalised D₂O solvent scattering. It can be seen in Figure 6 and here that the incoherent background scattering is slightly higher for the gel phase data than for the solution data at the same 2NapFF concentration of 0.5 wt%. Owing to its large incoherent cross-section the contribution from hydrogenous material within the sample dominates the background scattering. The same solvent (D₂O) background was subtracted from both data sets, however, it is possible that the slightly raised background could come from exchange of D₂O to H₂O either in the sample solution or in the Ca salt solution that was added to induce gelation. The incoherent cross-section of Ca is very low and therefore its presence is unlikely to have caused the increase in background.

	0.3% solution	0.4% solution	0.5% solution	0.5% gel
Power law scale (/10 ⁻⁵)	7±2	0.5±0.4	1.7±0.3	15±4
Power law value, N	2.2±0.2	3.1±0.2	2.47±0.08	2.14±0.08
Cylinder scale (/10 ⁻³)	0.20±0.04	0.95±0.05	1.8±0.4	1.8±0.3
Radius, R (nm)	3.5±0.5	3.7±0.3	3.7±0.3	3.7±0.3
Inner core radius, R_{core} (nm)	1.6±0.4	1.6±0.3	1.6±0.3	-
Kuhn length (nm)	-	-	-	19±3
Length, L (nm)	-	-	-	43±3
Hollow length, L_H (nm)	>50	>50	50±10	-
Background (cm⁻¹)	0.045±0.005	0.050±0.005	0.0010±0.0005	0.007±0.002

Table S1. The model fit parameters generated by fitting the customised hollow and flexible cylinder models to the data in SasView. Uncertainties were estimated by fixing certain key parameters as mentioned above.

References

1. Z. Lin, J. J. Cai, L. E. Scriven and H. T. Davis, *The Journal of Physical Chemistry*, 1994, **98**, 5984-5993.
2. C. A. Dreiss, *Soft Matter*, 2007, **3**, 956-970.
3. www.sasview.org.
4. L. A. Feigin and D. I. Svergun, *Structure Analysis by Small-Angle X-Ray and Neutron Scattering*, Plenum Press, New York, 1987.
5. J. S. Pedersen and P. Schurtenberger, *Macromolecules*, 1996, **29**, 7602-7612.
6. W.-R. Chen, P. D. Butler and L. J. Magid, *Langmuir*, 2006, **22**, 6539-6548.
7. A. Guinier and G. Fournet, *Small Angle Scattering of X-rays*, 1955.
8. K. L. Morris, L. Chen, J. Raeburn, O. R. Sellick, P. Cotanda, A. Paul, P. C. Griffiths, S. M. King, R. K. O'Reilly, L. C. Serpell and D. J. Adams, *Nature Communications*, 2013, **4**.